ADVANCED MATERIALS
www.advmat.de

Room-Temperature Ferroelectricity in Ultra-Thin p-Type BiCuSeO Films

Lingyuan Kong, Wei Li, Zihao Wang, Zixin Fan, Zhuo Yin, Haoming Ling, Kai Hu, Shaojie Tai, Dingyi Li, Chengkai Li, Yang Guo, Fang Yang, Wei Zhang, Jiandong Guo, Runzhang Xu, Pan Chen,* Yan Liang,* and Jiandi Zhang**

Atomically thin 2D layered ferroelectric semiconductors, where polarization switching transpires within the channel material itself, are pivotal to advancing the next generation of high-performance electronics. Nevertheless, the challenge remains in either the controllable synthesis of films or the manipulation of associated ferroelectricity. Here, 2D p-type BiCuSeO (BCSO) films with a thickness down to ≈3 nm are successfully synthesized using molecular beam epitaxy. The room-temperature (RT) out-of-plane ferroelectricity is confirmed by piezoelectric force microscopy, showing robust ferroelectric switching capability. Insights derived from density functional theory, coupled with the ferroelectric dipole map in cross-sectional scanning transmission electron microscopy images, suggest that the polar displacement of [CuSe] layers under electric fields primarily contributes to ferroelectricity in the BCSO film. Furthermore, the switching behavior of the BCSO-based ferroelectric tunnel junction has been clarified, exhibiting distinct ON and OFF states. Our results illustrate that such an ultrathin RT ferroelectric semiconductor could serve as a versatile material for future multifunctional electronic devices.

1. Introduction

Ferroelectricity, characterized by electric polarization that can be tuned by ambient electric field, has captured rising attention due to its potential applications in advanced nanoelectronics with multifunctionalities.[1] While most ferroelectric materials, including polyvinylidene fluoride[2] or perovskite oxides,[3,4] have a wide bandgap and poor carrier mobility. These characteristics impose obstacles to their multifunctional application. Although ferroelectric/semiconductor heterostructures facilitate the development of innovative devices,[5,6] their polarization switching is confined to dielectric layers, which impedes channel control. On the contrary, 2D ferroelectric materials permit direct polarization switching within the conductive channel,[7,8] presenting inherent advantages for electronics at the atomic scale. In recent experiments, atomically thin SnTe[9] and Bi_2TeO_5[10] have exhibited in-plane room-temperature (RT) ferroelectric responses, while metal thiophosphate,[11,12] In_2Se_3,[13] 1T MoS_2,[14] and Bi_2O_2Se (BOS)[15,16] demonstrated out-of-plane ferroelectric response. Among these, BOS stands out as particularly promising due to its superior properties, including moderate bandgap size, high electron mobility, and remarkable ambient stability.[17] However, the development of 2D p-n junction architecture, along with the exploration of tunneling field effect transistor devices, is currently constrained by the limited research on the corresponding 2D p-type semiconductors.[18,19] Recent developments in 2D ferroelectric materials have primarily focused on n-type 2D materials, with a noticeable absence of ferroelectric p-type semiconductors.

BiCuSeO (BCSO), a typical p-type semiconductor, shares nearly the same in-plane crystal structure and lattice constant as BOS,[20] facilitating the fabrication of 2D p-n heterostructures. BCSO has a band gap of ≈0.8 eV and a low intrinsic thermal conductivity of roughly 0.6 $Wm^{-1}K^{-1}$ at room temperature (RT), which is considered to be a highly promising thermoelectric conversion material.[21] Research has demonstrated that the inherent p-type heavy doping and stable chemical properties of BCSO make it a valuable asset for interface regulation in 2D

L. Kong, W. Li, Z. Wang, Z. Fan, Z. Yin, H. Ling, K. Hu, S. Tai, D. Li, C. Li, Y. Guo, F. Yang, J. Guo, P. Chen, Y. Liang, J. Zhang
Beijing National Laboratory for Condensed Matter Physics
Institute of Physics
Chinese Academy of Sciences
Beijing 100190, China
E-mail: panch@iphy.ac.cn; liangyan_sf6i@iphy.ac.cn; jiandiz@iphy.ac.cn

L. Kong, W. Li, W. Zhang
Hebei Key Lab of Optic-electronic Information and Materials
College of Physics Science and Technology
Hebei University
Baoding 071002, China

R. Xu
Department of Physics
The Hong Kong University of Science and Technology
Hong Kong 999077, China
E-mail: xurz@ust.hk

J. Guo, J. Zhang
College of Physics
University of Chinese Academy of Sciences
Beijing 100190, China

The ORCID identification number(s) for the author(s) of this article can be found under https://doi.org/10.1002/adma.202510566

DOI: 10.1002/adma.202510566

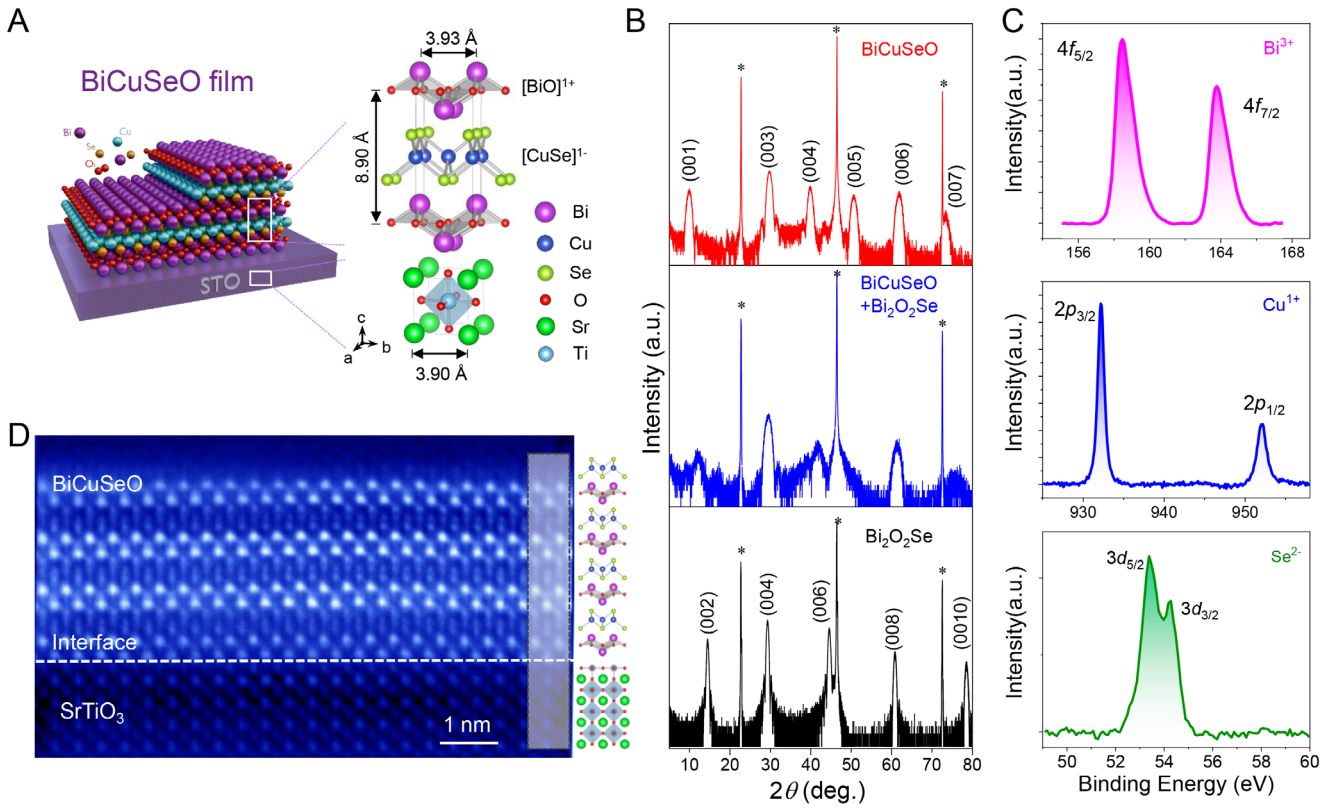

Figure 1. Preparation and physical characterization of BCSO films. A) Left: schematic diagram of layer-by-layer growth of the atomically thin BCSO film on a (001)-oriented STO substrate by co-evaporating the Bi, Cu, and Se precursors in an oxygen atmosphere. Right: the crystal structure of BCSO and STO. B) XRD pattern of the BOS (bottom), BCSO (top) films, and their mixed phase (middle). The asterisks indicate the peaks of STO substrates. C) XPS spectra of Bi, Cu, and Se elements in BCSO thin films. D) Cross-sectional HAADF-STEM image of the BCSO film on a STO substrate, accompanied by an atomic model.

heterostructures,[22–24] thus showing potential use in optoelectronic devices.[25,26] Moreover, the unique self-modulating doping effect mechanism of BCSO enables it to retain its degeneracy even when its thickness is reduced to a mere few layers,[26,27] which shows advantages in the fabrication of high-speed, low-power 2D-2D thin-film transistors. However, the growth of BCSO films, particularly ultra-thin versions, still presents substantial challenges. Recent advancements have enabled the preparation of BCSO films through methods such as pulsed laser deposition (PLD),[28] chemical vapor deposition (CVD),[21] and solvothermal synthesis.[29] Nevertheless, each of these methods exhibits certain limitations. For instance, the surface of PLD-grown BCSO thin films is not flat enough. Both the CVD and solvothermal methods exhibit limitations in generating BCSO nanosheets of a relatively small size. Moreover, the literature regarding ferroelectricity in p-type BCSO thin films is notably absent.

In this work, we have successfully grown atomically thin BCSO films via molecular beam epitaxy (MBE), which was accomplished by co-evaporating Bismuth (Bi), Copper (Cu), and Selenium (Se) precursors within an oxygen atmosphere. The BCSO films demonstrate semiconductor properties with p-type carriers, exhibiting an elevated carrier density of 2.62×10^{14} cm^{-2} at RT. Notably, this density surpasses that of numerous well-established p-type 2D semiconductors.[11,12] The intrinsic ferroelectric transitions have been revealed by piezoelectric force microscopy (PFM) signals, exhibiting typical butterfly curves in amplitude and 180° switching in phase. This is corroborated by the processes of writing/reading ferroelectric domains within BCSO films. Further analyses, as evidenced by the first-principles density functional theory (DFT) results combined with the ferroelectric dipole map in the cross-sectional scanning transmission electron microscopy (STEM) image, suggest that the displacement of [CuSe] under an electric field is primarily responsible for the ferroelectricity observed in BCSO films. Additionally, the switching behavior of 2D BCSO has been further clarified utilizing a conducting tip/BCSO/Nb-$SrTiO_3$ ferroelectric tunnel junction (FTJ) device, showing a distinct ON/OFF switching performance.

2. Results and Discussion

BCSO, with a ZrSiCuAs-type crystal structure ($I4/nmm$, $a = b =$ 3.93 Å, $c = 8.90$ Å), consists of alternating [BiO] and [CuSe] layers along the out-of-plane orientation (**Figure 1A**). We selected single polished TiO_2-terminated $SrTiO_3$ (STO) (001) single crystals, which have a cubic structure ($a = 3.90$ Å) and high thermal stability, as the epitaxial substrates. STO offers a reasonable lattice match to BCSO, with a mismatch of ≈0.7 %. The fabrication of atomically thin BCSO films is accomplished using a custom-built oxide MBE setup. The MBE of BCSO presents

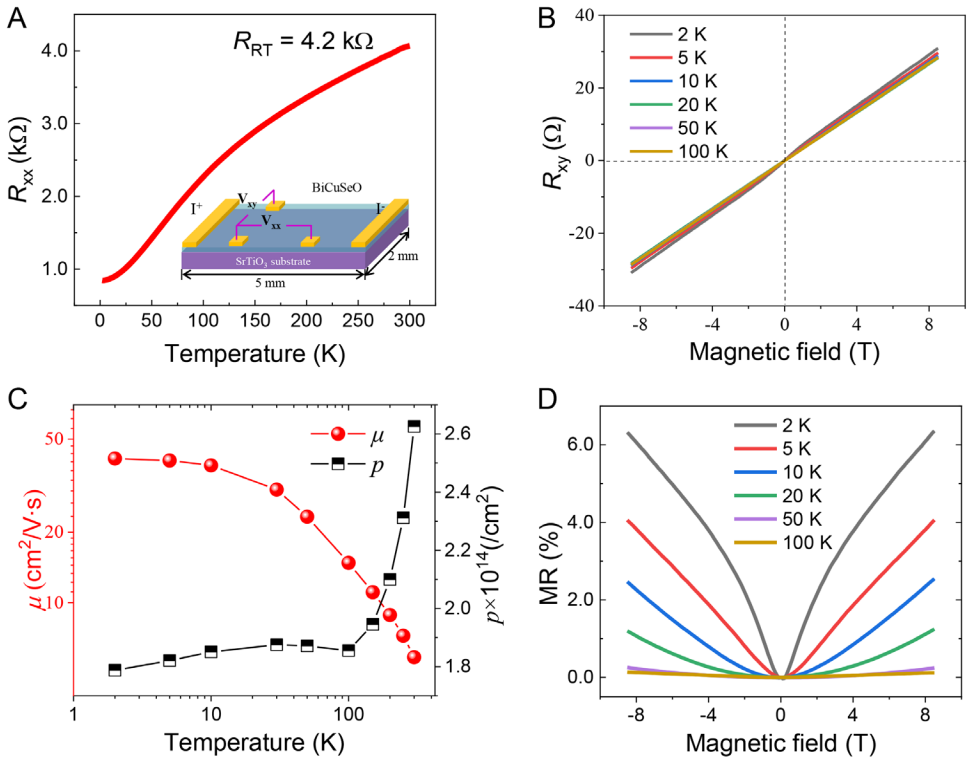

Figure 2. Transport properties of BCSO films. A) Temperature-dependent sheet resistance R_{xx} of the BCSO film. B) Magnetic field dependence of Hall resistance R_{xy} of the BCSO film at various temperatures. C) Carrier mobility μ and carrier density p, derived from Hall measurements using a single band model, versus temperatures. D) Magnetic field dependence of MR of the BCSO film at various temperatures.

significant challenges due to the fact that BCSO is a quaternary compound. Managing four elements in conjunction with the substrate temperature requires a high level of precision, making it particularly difficult. Given the structural parallels between BOS and BCSO, and our previous research on the growth of oxygen-sulfur compounds by MBE,[20] we tried to incorporate Cu into the BOS growth process to facilitate the fabrication of BCSO thin films. The bottom layer of Figure 1B depicts the X-ray diffraction (XRD) pattern of the BOS film, which exhibits a (00*l*) orientation. When Cu is directly integrated under the BOS growth conditions, a mixed phase of BOS and BCSO emerges, as represented in the middle layer of Figure 1B. A comprehensive description of the mixed phase is provided in (Figure S1, Supporting Information). By simultaneously decreasing the evaporation rate of Bi and increasing the substrate temperature, we can achieve a pure-phase BCSO film, represented as the top layer in Figure 1B. Sharp diffraction peaks and distinct Laue oscillation peaks are observed in the XRD, confirming the high crystal quality and layer-by-layer growth pattern of BCSO films. This layer-by-layer growth mode is further corroborated by atomic force microscope (AFM) results, as depicted in Figure S2 (Supporting Information).

The X-ray photoelectron spectroscopy (XPS) technique was employed to unveil the elemental composition and chemical bonding states of the MBE-grown BCSO films. As illustrated in Figure 1C, the peaks of Bi $4f_{7/2}$ and Bi $4f_{5/2}$ are positioned at 158.9 and 164.2 eV, respectively, indicating the valence state of Bi^{3+}. For the Cu element, two peaks situated at 932.1 and 951.8 eV are designated as Cu $2p_{3/2}$ and Cu $2p_{1/2}$, indicating a valence state of Cu^{1+}. Significant split spin-orbit component of 13.7 eV is in accord well with the theoretical value. Notably, the film exhibits no peak for Cu with a valence state of Cu^{2+}, indicating the excellent air-stability of the BCSO film under ambient conditions. The XPS results for the Se element are presented in the lower layer of Figure 1C, indicating a Se^{2-} state. To study the crystal quality of the MBE-grown BCSO film, we performed systematic characterization of cross-sectional STEM on the sample (Figure 1D). High-angle annular dark-field (HAADF)-STEM images show an atomically sharp interface between BCSO and STO, where strongly bonded heterointerfaces with strict epitaxial growth are revealed. The layered BCSO, which has a thickness of ≈4 u.c. (≈3 nm), exhibits a stacked structure comprising [BiO] and [CuSe] units. These findings highlight the layered configuration and high crystalline quality of the BCSO film, both of which are critical for exploring its electronic properties.

The transport characteristics of ultrathin BCSO films were measured utilizing a Hall device with dimensions of 5 mm × 2 mm (**Figure 2**A, inset). As illustrated in Figure 2A, the sheet resistance-temperature (R_{xx}–T) curve for the BCSO gradually decreases as the temperature drops from 300 to 2 K. This suggests that BCSO is in a doped state, which is induced by the presence of Cu vacancies.[30] The slight hump observed between 100 and 150 K in the R_{xx}–T curve can potentially be associated with a phase crossover of BCSO.[21] Notably, at 300 K, the in-plane resistance of BCSO is ≈4 KΩ; however, the BCSO displays an elevated out-of-plane resistance exceeding 10 MΩ when measured at low voltage. In short, the MBE-grown BCSO film is metallic in-plane and

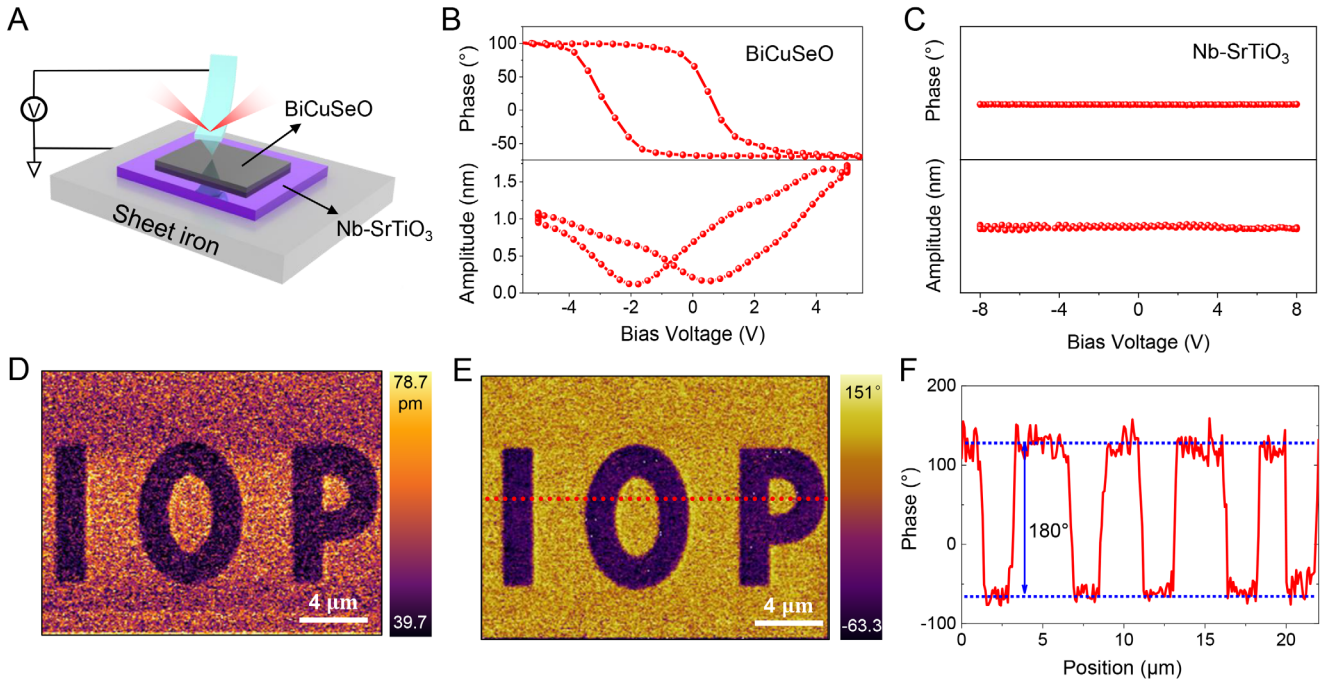

Figure 3. Out-of-plane ferroelectricity in ultrathin BCSO film. A) Schematic diagram of the PFM measurement setup. B) Off-field PFM phase and amplitude loops for BCSO film and C) a bare STO substrate, respectively. D) The amplitude and E) phase images obtained after writing an opposite DC bias "IOP" pattern using PFM. F) The phase lag curve of the BCSO at the red dashed line position.

insulating out-of-plane, which enables the existence of out-of-plane ferroelectricity and device application. Figure 2B depicts the correlation between Hall resistance (R_{xy}) and the magnetic field of a BCSO film at varying temperatures. The relationship between Hall resistance and the magnetic field, characterized by a quasi-linear and positive slope, indicates that transport at varying temperatures is dominated by hole carriers. This evidence substantiates the assertion that BCSO is a p-type semiconductor. It should be pointed out that the Hall curves for 2 and 5 K are not entirely linear, suggesting the potential presence of a minor concentration of n-type carriers. By comparing the fitting results of two-carrier and single-carrier models, and consulting relevant literature [31] we opted for the single-carrier approach (see Figure S3, Supporting Information for details). At 2 K, the carrier density, denoted as p, has a value of 1.78×10^{14} cm^{-2}, increases with increasing temperature, and reaches 2.62×10^{14} cm^{-2} at 300 K (represented by the black square line in Figure 2C). The high carrier density is conductive to the fabrication of high-performance tunneling FET devices. The red ball line in Figure 2C illustrates the temperature-dependent variation of the carrier mobility, represented as μ. At 2 K, μ has the maximum value of 41.28 $cm^2\ V^{-1}{\cdot}s^{-1}$, while it drops to 5.85 $cm^2\ V^{-1}{\cdot}s^{-1}$ at 300 K. Such a decrease in mobility with increasing temperature may be attributed to phonon scattering. Figure 2D illustrates the magnetoresistance (MR) of the BCSO film in a vertical magnetic field at varying temperatures. The definition of MR can refer to the literature.[32] At low temperatures, a weak anti-localization (WAL) effect is evident in the thin film. With increasing measurement temperature, the WAL effect weakens, reverting to the parabolic structure governed by classical orbital action and electron-electron interaction.

The investigation of RT out-of-plane ferroelectricity in ultrathin BCSO films is conducted through a comprehensive array of PFM measurements. The experimental setup of the PFM measurements is shown in **Figure** 3A. An Nb-doped STO substrate was used as a conductive substrate to reduce charge accumulation. Typically, applying a minor voltage to the AFM tip induces uniform dipole moment orientation in ferroelectric materials when subjected to a vertical electric field.[33,34] For the standard hysteresis measurement, a triangular voltage waveform is applied. The off-field signal is measured in the interval between two pulsed bias voltages. We recorded off-field phase and amplitude loops for a thin BCSO film, as illustrated in Figure 3B. A butterfly loop, accompanied by 180° phase switching, has been observed. Notably, the amplitude and phase results of the PFM demonstrate well repeatability (Figure S4, Supporting Information). In contrast, PFM signals display flat and nonhysteretic lines when indented on an Nb-doped STO substrate, prepared under identical conditions with the exception of film growth (Figure 3C). It is intriguing to attribute the observation of ferroelectricity to the BCSO film rather than the Nb-doped STO substrate. Additionally, within the Supporting Information, we have discussed and ruled out the influence of surface adsorption on ferroelectricity. Subsequently, we used dual AC resonance-tracking PFM (DART-PFM) characterization to investigate the ferroelectric switching properties of the thin BCSO film. Following the application of a ±9 V DC voltage to the BCSO film for the "IOP" pattern writing, distinct bright and dark regions were clearly observable in both the PFM amplitude and phase images. (Figure 3D,E). Moreover, the phase lag curve of the PFM phase image at the red dashed line position showed a 180° phase contrast (Figure 3F). Together, all the results indicate the robust ferroelectric switching feature of

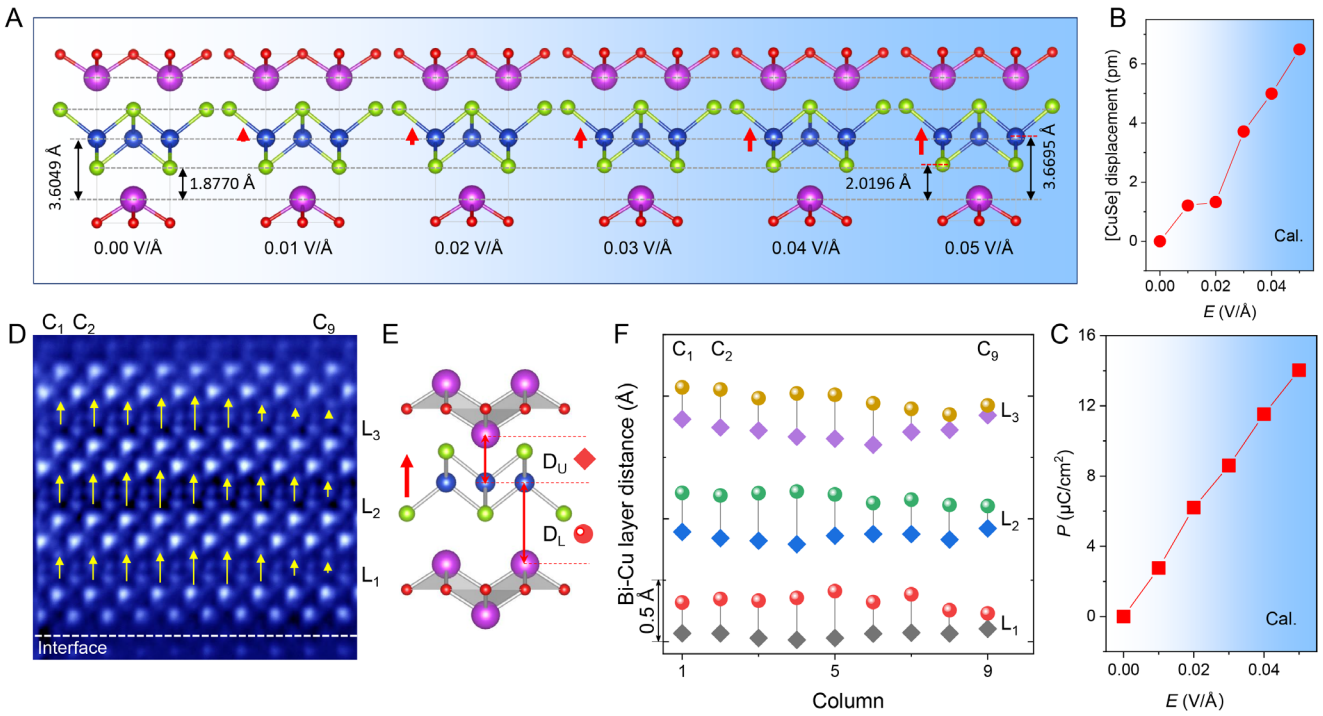

Figure 4. DFT calculations and STEM results of the polar characteristic in the thin BCSO film. A) BCSO crystal structures under different electric fields from 0.00 to 0.05 V Å^{-1}. The red arrows schematically show the polar displacement of [CuSe]. B) The calculated [CuSe] displacement as a function of vertical electric field. C) The calculated vertical polarization as a function of vertical electric field. D) Cross-sectional HAADF-STEM image of BCSO film with [CuSe] displacement included. E) A schematic diagram of the [CuSe] shift, with "D_U" represented as a "rhombus" and "D_L" depicted as a "sphere". F) Computational D_U and D_L values for the STEM image of (D), wherein L_1 to L_3 denote three layers and C_1 to C_9 represent nine columns.

BCSO, which lays the foundation for potential ferroelectric applications.

To elucidate the underlying physics of the ferroelectricity in BCSO films, we executed simulations utilizing first-principles DFT. In pristine bulk BCSO, the interplanar distances between the adjacent [BiO] and [CuSe] layers are exactly the same. Upon the application of a vertical electric, a marked displacement of the [CuSe] layer in BCSO is observed in the direction of the field with respect to [BiO], as schematically shown by the red arrows in **Figure** 4A. Although both Cu and Se sublayers in the [CuSe] layer are displaced with different amounts, for the alignment with experimental results, we selectively use Cu displacement as a representative for the displacement of the entire [CuSe] layer. Clearly, the displacement of the [CuSe] layer has a strong and positive dependence on the field strength, reaching as high as ≈7 pm under an electric field of 0.05 V Å^{-1} (Figure 4B). Meanwhile, the vertical polarization also shows a positive relationship with field strength, achieving 14 μC cm^{-2} under an electric field of 0.05 V Å^{-1} (Figure 4C). Such polarization originates from the interplay between electric field-driven deformation of structures and redistribution of charges and can be sustained for a noticeable relaxation time, which potentially gives rise to ferroelectric hysteresis.[35]

In the cross-sectional STEM study, we did observe the symmetry breaking of BCSO, which resulted in an initial polarization (Figure 4D). To accurately determine the polar displacement of the [CuSe] layer, we quantified the distance between the Cu atom and its neighboring Bi atoms in BCSO in STEM images, denoted as "D", which can reflect the spacing between the [CuSe] and the adjacent [BiO] layers, as illustrated in Figure 4E. In one BCSO layer, the D values are designated as "D_U, rhombus" for the distance between the upper [BiO] layer and the [CuSe] layer, and as "D_L, sphere" for the distance between the lower [BiO] layer and the [CuSe] layer (Figure 4E). Moreover, to ensure the accuracy of our computations, we calculated D values for three BCSO layers, denoted as L_1 through L_3, and nine sequential BCSO columns, designated as C_1 through C_9. A detailed explanation of the calculation method is included in Figure S5 (Supporting Information). The computational results are depicted in Figure 4F. These findings reveal a marked consistency in values within each column and layer of the BCSO film, with D_L consistently exceeding D_U, illustrating the displacement of the [CuSe] layer. To more effectively observe the displacement of the [CuSe] layer, the movement of each [CuSe] was computed, amplified 20-fold, and then highlighted on the STEM map (Figure 4D). The displacement values for [CuSe] are provided quantitatively in Table S1 (Supporting Information). Upon calculating average values, it is found that the polar displacement of the [CuSe] layer is ≈14 pm. This magnitude aligns with the calculated result and is notably similar to the Ti-O polar displacements observed in $BaTiO_3$,[36] a well-established ferroelectric material.

To demonstrate the possible applications of ferroelectric BCSO layers, such as nonvolatile memories, a BCSO-based FTJ device was fabricated. As schematically shown in **Figure** 5A, asymmetrical electrodes consist of a 0.5 mm thick Nb-STO on the bottom and a tungsten tip electrode on the top, while a 3 nm-thick BCSO

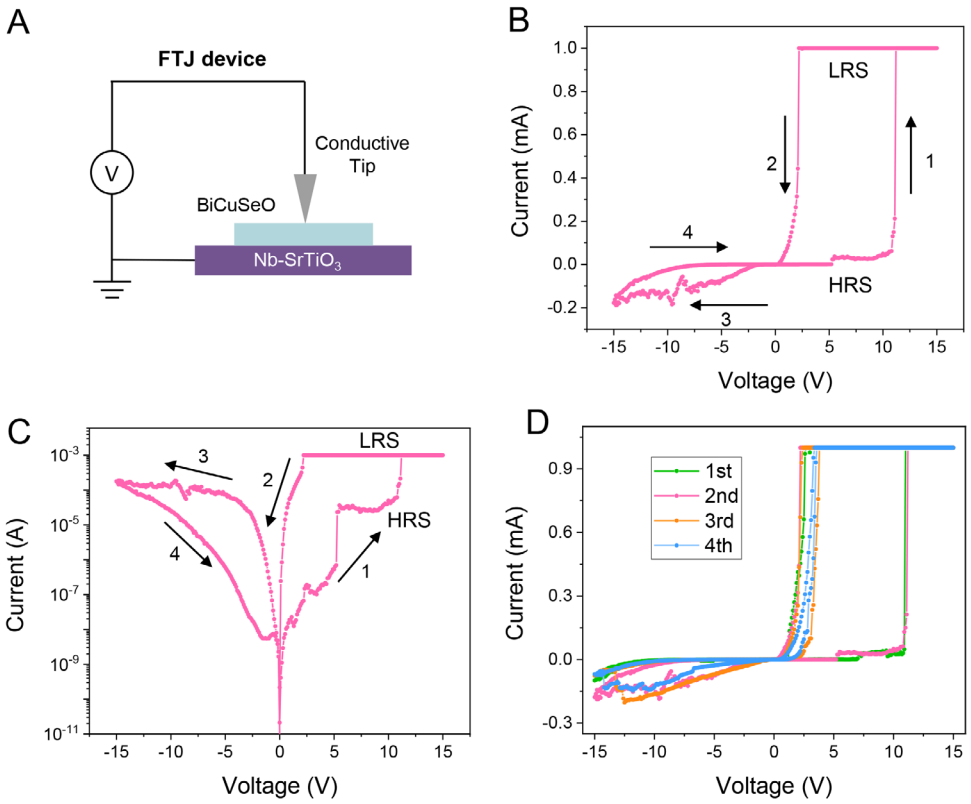

Figure 5. BCSO-based FTJ device. A) Schematic experimental setup for conductive tip/BCSO/Nb-STO device measurements, in which the BCSO film acts as the polarity switching medium. *I–V* curves with current in B) linear scale and C) logarithmic scale at 300 K. D) Consecutive *I–V* semi-cycle sweeping.

is sandwiched between them to form the ferroelectric tunnel barrier. The *I–V* curves, depicted at 300 K in both linear and logarithmic scales (Figure 5B,C), clearly indicate a unique polarity switching behavior. Two distinct resistance states are distinguished, in which the low-resistance state (LRS) and high-resistance state (HRS) represent the ON and OFF states of the device. Under the 0 to 11 V forward sweep (process 1), the BCSO is at a HRS, and then switches to LRS during the sweep from 11 to 0 V (process 2). Next, the negative electric field sweep from 0 to −15 V (process 3) and recovered to HRS under the −15 to 0 V sweep (process 4). Furthermore, consecutive semicycle sweeping (0 V→−15 V→0 V→15 V→0 V) was performed (Figure 5D), revealing a reduction in the conductive window as the semicycle sweeping increased. We suppose that the resistance switching process in BCSO films may be attributed to ferroelectric switching, coupled with the formation and rupture of conductive filaments (see the Supporting Information for a comprehensive discussion). These results can serve as a proof-of-concept demonstration for the potential application of 2D BCSO in FTJ devices operating at RT.

3. Conclusion

We demonstrated the MBE-growth of atomically thin BCSO films down to ≈3 nm by co-evaporating Bi, Cu, and Se precursors in an oxygen atmosphere. The RT ferroelectricity of BCSO films is evidenced by PFM signals, which exhibit typical butterfly curves in amplitude and 180° phase switching, along with domain writing/reading capabilities. DFT calculations together with ferroelectric dipole map in STEM image demonstrate that the displacement of [CuSe] under electric fields is the primary source of ferroelectricity in BCSO films. Furthermore, the switching behavior of the BCSO-based FTJ has been elucidated using a conducting tip/BCSO/Nb-STO device, demonstrating distinct ON and OFF states. Our study represents a significant advancement in the realization of RT p-type ferroelectric semiconductor, offering a promising avenue for future device applications.

4. Experimental Section

Sample Preparation: BCSO films were grown on TiO_2-terminated STO substrates using MBE. The STO substrates, exhibiting a singular TiO_2 termination, were prepared through high-temperature annealing in ultra-high vacuum followed by low-temperature oxygenation. The growth sources for the BCSO film comprised high-purity particles of Bismuth (Bi), Cuprum (Cu), and Selenium (Se) with a purity of 99.999%. The evaporation of Bi, Cu, Se, and the precursor was performed in an oxygen-rich environment of 1.2×10^{-4} mbar. Bi, Cu, and Se were evaporated using oxygen-resistant sources, with source evaporation temperatures set at 520, 1080, and 184 °C, respectively. The growth process commences with the introduction of oxygen into the vacuum chamber, followed by increasing the substrate temperature to the optimal growth temperature of 510 °C. Subsequently, the shutters of Bi, Cu, and Se sources are simultaneously opened. Following the completion of film growth, the three shutters were closed first, after which the sample was cooled to RT within an oxygen

atmosphere. Subsequent to this growth procedure, the BCSO films demonstrated precise layer-by-layer growth control.

Sample Characterization: The crystal structures of samples were analyzed at RT by XRD (Rigaku Smart Lab) with a Ge (220) × 2 crystal monochromator. The chemical valence states of the films were characterized by XPS (Thermo Scientific ESCALAB 250). The electrical transport measurements were performed in a Physical Property Measurement System (PPMS, Quantum Design) with the Hall device. In the process of electrode fabrication for Hall devices, we utilized indium metal and melted it with a welding gun. The surface morphology and ferroelectric switching were performed in an AFM system (Asylum ES, Oxford). Cross-sectional STEM samples were prepared by focused-ion beam equipment (Helios 5CX) with Ga ions. STEM characterization was performed in a double aberration-corrected JEOL Grand ARM 300F microscope.

DFT Calculations: The first-principles DFT results were calculated by using the Vienna ab-initio Simulation Package (VASP).[37,38] The exchange correlations and the ion-electron interactions were treated by the Perdew-Burke-Ernzerhof (PBE) functional[39] and the projected-augmented wave (PAW).[40,41] The energy and force convergence criteria for the relaxation of crystal structures were 1×10^{-5} eV and −0.01 eV Å^{-1}, respectively. The plane wave cutoff was set as 500 eV, the k-point sampling in relaxations uses 13×13×5 under Monkhorst-Pack scheme,[42] while increasing to 17 × 17 × 7 in electronic structure calculations. The electric field-induced relaxation was implemented by adding the multiplication of born effective charge and the electric field to VASP force optimizations.[43–45] The electric polarization was obtained by using the modern theory of polarization.[46]

Supporting Information

Supporting Information is available from the Wiley Online Library or from the author.

Acknowledgements

L.K. and W.L. contributed equally to this work. This work was supported by the National Key Research and Development Program of China (Grant No. 2024YFF0508500, 2022YFA1403000), the National Natural Science Foundation of China (Grant No. 12204522, 12434007, 12250710675, and U23A20366), and the Post-graduate's Innovation Fund Project of Hebei University (HBU2025SS033).

Conflict of Interest

The authors declare no conflict of interest.

Data Availability Statement

The data that support the findings of this study are available from the corresponding author upon reasonable request.

Keywords

2D ferroelectric semiconductor, Bi_2O_2Se, BiCuSeO, molecular beam epitaxy, p-type semiconductor

Received: June 4, 2025
Revised: August 11, 2025
Published online:

[1] W. Eerenstein, N. D. Mathur, J. F. Scott, *Nature* **2006**, *442*, 759.
[2] Prateek, V. K. Thakur, R. K. Gupta, *Chem. Rev.* **2016**, *116*, 4260
[3] N. A. Spaldin, *Science* **2004**, *304*, 1606.
[4] I. Grinberg, D. V. West, M. Torres, G. Gou, D. M. Stein, L. Wu, G. Chen, E. M. Gallo, A. R. Akbashev, P. K. Davies, J. E. Spanier, A. M. Rappe, *Nature* **2013**, *503*, 509.
[5] S. Y. Yang, J. Seidel, S. J. Byrnes, P. Shafer, C.-H. Yang, M. D. Rossell, P. Yu, Y.-H. Chu, J. F. Scott, J. W. Ager, L. W. Martin, R. Ramesh, *Nat. Nanotechnol.* **2010**, *5*, 143.
[6] M. Si, A. K. Saha, S. Gao, G. Qiu, J. Qin, Y. Duan, J. Jian, C. Niu, H. Wang, W. Wu, S. K. Gupta, P. D. Ye, *Nat. Electron.* **2019**, *2*, 580.
[7] Z. Fei, W. Zhao, T. A. Palomaki, B. Sun, M. K. Miller, Z. Zhao, J. Yan, X. Xu, D. H. Cobden, *Nature* **2018**, *560*, 336.
[8] D. Akinwande, C. Huyghebaert, C. H. Wang, M. I. Serna, S. Goossens, L. J. Li, H. P. Wong, F. H. L. Koppens, *Nature* **2019**, *573*, 507.
[9] K. Chang, J. Liu, H. Lin, N. Wang, K. Zhao, A. Zhang, F. Jin, Y. Zhong, X. Hu, W. Duan, Q. Zhang, L. Fu, Q.-K. Xue, X. Chen, S.-H. Ji, *Science* **2016**, *353*, 274.
[10] M. Han, C. Wang, K. Niu, Q. Yang, C. Wang, X. Zhang, J. Dai, Y. Wang, X. Ma, J. Wang, L. Kang, W. Ji, J. Lin, *Nat. Commun.* **2022**, *13*, 5903.
[11] W. F Io, S. Y. Pang, L. W. Wong, Y. Zhao, R. Ding, J. Mao, Y. Zhao, F. Guo, S. Yuan, J. Zhao, J. Yi, J. Hao, *Nat. Commun.* **2023**, *14*, 7304
[12] F. C. Liu, L. You, K. L. Seyler, X. Li, P. Yu, J. Lin, X. Wang, J. Zhou, H. Wang, H. He, S. T. Pantelides, W. Zhou, P. Sharma, X. Xu, P. M. Ajayan, J. Wang, Z. Liu, *Nat. Commun.* **2016**, *7*, 12357
[13] W. Han, X. Zheng, K. Yang, C. S. Tsang, F. Zheng, L. W. Wong, K. H. Lai, T. Yang, Q. Wei, M. Li, W. F. Io, F. Guo, Y. Cai, N. Wang, J. Hao, S. P. Lau, C.-S. Lee, T. H. Ly, M. Yang, J. Zhao, *Nat. Nanotechnol.* **2023**, *18*, 55.
[14] X. R. Wang, K. Yasuda, Y. Zhang, S. Liu, K. Watanabe, T. Taniguchi, J. Hone, L. Fu, P. J. Herrero, *Nat. Nanotechnol.* **2022**, *17*, 367.
[15] M. Q. Wu, Z. F. Lou, C. M. Dai, T. Wang, J. Wang, Z. Zhu, Z. Xu, T. Sun, W. Li, X. Zheng, X. Lin, *Adv. Mater.* **2023**, *35*, 2300450.
[16] L. Tang, L. Dang, M. Han, S. Li, U. Khan, W. Chen, Z. Cai, L. Kong, Q. Wu, B. Liu, Q. Zhang, R. Xu, X. Ma, *Adv. Funct. Mater.* **2024**, *34*, 2405898.
[17] J. X. Wu, H. T. Yuan, M. Meng, C. Chen, Y. Sun, Z. Chen, W. Dang, C. Tan, Y. Liu, J. Yin, Y. Zhou, S. Huang, H. Q. Xu, Y. Cui, H. Y. Hwang, Z. Liu, Y. Chen, B. Yan, H. Peng, *Nat. Nanotechnol.* **2017**, *12*, 530.
[18] R. Yan, S. Fathipour, Y. Han, B. Song, S. Xiao, M. Li, N. Ma, V. Protasenko, D. A. Muller, D. Jena, H. G. Xing, *Nano Lett.* **2015**, *15*, 5791.
[19] D. Sarkar, X. Xie, W. Liu, W. Cao, J. Kang, Y. Gong, S. Kraemer, P. M. Ajayan, K. Banerjee, *Nature* **2015**, *526*, 91.
[20] Y. Liang, Y. Chen, Y. Sun, S. Xu, J. Wu, C. Tan, X. Xu, H. Yuan, L. Yang, Y. Chen, P. Gao, J. Guo, H. Peng, *Adv. Mater.* **2019**, *31*, 1901964.
[21] J. Li, Y. Zhang, J. Zhang, J. Chu, L. Xie, W. Yu, X. Zhao, C. Chen, Z. Dong, L. Huang, L. Yang, Q. Yu, Z. Ren, J. Wang, Y. Xu, K. Zhang, *Adv. Mater.* **2022**, *34*, 2207796.
[22] G. K. Ren, S. Wang, Z. Zhou, X. Li, J. Yang, W. Zhang, Y. H. Lin, J. Yang, C.-W. Nan, *Nat. Commun.* **2019**, *10*, 2814.
[23] D. Feng, F. Zheng, D. Wu, M. Wu, W. Li, L. Huang, L.-D. Zhao, J. He, *Nano Energy* **2016**, *27*, 167.
[24] J. L. Lan, C. Deng, W. Ma, G.-K. Ren, Y.-H. Lin, X. Yang, *J. Alloys Compd.* **2017**, *708*, 955.
[25] C. Barreteau, L. Pan, E. Amzallag, L. D. Zhao, D. Bérardan, N. Dragoe, *Semicond. Sci. Tech.* **2014**, *29*, 064001.
[26] J. Gamon, D. Giaume, G. Wallez, J.-B. Labégorre, O. I. Lebedev, R. Al Rahal Al Orabi, S. Haller, T. Le Mercier, E. Guilmeau, A. Maignan, P. Barboux, *Chem. Mater.* **2018**, *30*, 549.
[27] G. H. Shin, B. Koo, H. Park, Y. Woo, J. E. Lee, S.-Y. Choi, *ACS Appl. Mater. Interfaces* **2018**, *10*, 40212.
[28] X. Wu, L. Gao, P. Roussel, E. Dogheche, J. Wang, G. Fu, S. Wang, *J. Am. Ceram. Soc.* **2016**, *99*, 3367.
[29] M. Samanta, S. N. Guin, K. Biswas, *Inorg. Chem. Front.* **2017**, *4*, 84.

[30] Y. Liu, L.-D. Zhao, Y. Liu, J. Lan, W. Xu, F. Li, B.-P. Zhang, D. Berardan, N. Dragoe, Y.-H. Lin, C.-W. Nan, J.-F. Li, H. Zhu, *J. Am. Chem. Soc.* **2011**, *133*, 20112.
[31] L. Zhang, Z. Li, Y. Deng, L. Li, Z. Gao, J. Chen, Z. Zhou, J. Huang, W. Xu, X. Fu, H. Yuan, F. Luo, J. Wu, *Nano Res.* **2023**, *16*, 10515.
[32] J. Xu, M. K. Ma, M. Sultanov, Z.-L. Xiao, Y.-L. Wang, D. Jin, Y.-Y. Lyu, W. Zhang, L. N. Pfeiffer, K. W. West, K. W. Baldwin, M. Shayegan, W.-K. Kwok, *Nat. Commun.* **2019**, *10*, 287.
[33] E. Soergel, *J. Phys. D: Appl. Phys.* **2011**, *44*, 464003.
[34] A. Gruverman, M. Alexe, D. Meier, *Nat. Commun.* **2019**, *10*, 1661.
[35] T. Birol, *Nature* **2018**, *560*, 174.
[36] G. S. Santolino, V. Rouco, S. Puebla, H. Aramberri, V. Zamora, M. Cabero, F. A. Cuellar, C. Munuera, F. Mompean, M. G. Hernandez, A. C. Gomez, J. Íñiguez, C. Leon, J. Santamaria, *Nature* **2024**, *626*, 529.
[37] G. Kresse, J. Furthmüller, *Comp. Mater. Sci.* **1996**, *6*, 15.
[38] G. Kresse, J. Furthmüller, *Phys. Rev. B* **1996**, *54*, 11169.
[39] J. P. Perdew, K. Burke, M. Ernzerhof, *Phys. Rev. Lett.* **1996**, *77*, 3865.
[40] P. E. Blöchl, *Phys. Rev. B* **1994**, *50*, 17953.
[41] G. Kresse, D. Joubert, *Phys. Rev. B* **1999**, *59*, 1758.
[42] P. Wisesa, K. A. McGill, T. Mueller, *Phys. Rev. B* **2016**, *93*, 155109.
[43] H. Fu, L. Bellaiche, *Phys. Rev. Lett.* **2003**, *91*, 057601.
[44] L. Chen, C. Xu, H. Tian, H. Xiang, J. Íñiguez, Y. Yang, L. Bellaiche, *Phys. Rev. Lett.* **2019**, *122*, 247701.
[45] H. J. Zhao, X. Liu, Y. Wang, Y. Yang, L. Bellaiche, Y. Ma, *Phys. Rev. Lett.* **2022**, *129*, 187602.
[46] R. Resta, *Rev. Mod. Phys.* **1994**, *66*, 899.